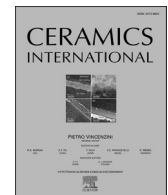




Contents lists available at ScienceDirect

Ceramics International

journal homepage: www.elsevier.com/locate/ceramint

Microwave-assisted hydrothermal synthesis of type II ZnSe/ZnO heterostructures as photocatalysts for wastewater treatment

M. Arellano-Cortaza^a, E. Ramírez-Morales^a, S.J. Castillo^b, L. Lartundo-Rojas^c, I. Zamudio-Torres^a, E.M. López Alejandro^a, L. Rojas-Blanco^{a,*}

^a Universidad Juárez Autónoma de Tabasco, Avenida Universidad s/n Zona de la Cultura, Colonia Magisterial, CP 86690, Villahermosa Centro, Tabasco, Mexico

^b Departamento de Investigación en Física, Universidad de Sonora, Blvd. Luis Encinas y Rosales S/N, Hermosillo, Sonora, 83000, Mexico

^c Instituto Politécnico Nacional, Centro de Nanociencias y Micro Nanotecnologías, Av. Luis Enrique Erro S/N, U.P. Adolfo Lopez Mateos, Gustavo A. Madero, C.P. 07738, Ciudad de Mexico, Mexico

ARTICLE INFO

Handling Editor: P. Vincenzini

Keywords:

Zinc oxide
Zinc selenide
Semiconductors
Photocatalyst
Heterostructure

ABSTRACT

The ZnSe/ZnO heterostructures were synthesized with the microwave-assisted hydrothermal method, using zinc acetate and zinc nitrate as a source of Zn²⁺ ions. Materials were characterized by X-ray diffraction (XRD), X-ray photoemitted electron spectroscopy (XPS), Raman spectroscopy, and scanning electron microscopy (SEM). The incorporation of ZnSe into the ZnO matrix produced changes both in the size of the ZnO crystallites and in the lattice parameters. Optical and texture analyses revealed that ZnSe particles cause a decrease in gap energy and a greater than 90% increase in the specific surface area of ZnSe/ZnO heterostructures compared to bare ZnO particles. ZnSe/ZnO heterostructures synthesized using zinc acetate as a Zn ion source exhibited better photocatalytic performance in visible light compared to pure ZnO.

1. Introduction

The use of renewable energies has become the current paradigm of research to produce green energy and avoid damage to the environment [1–3]. Semiconductor photocatalysis is one of the emerging technologies related to energy and environmental problems in a self-sustaining way [4]. Several factors influence the photocatalytic performance of materials, such as their specific surface area, the absorption capacity of visible light of the solar spectrum, their chemical and thermal stability, morphology, and crystallinity [5–7].

ZnO is an inexpensive, non-toxic material belonging to the family of group II-VI semiconductors, whose covalence is on the border between ionic and covalent semiconductors. This semiconductor, at room temperature, has an energy gap of 3.37 eV and an exit energy of ~60 meV [8], so it is used in optoelectronic devices and environmental applications due to its high photostability and large electrochemical coupling coefficients [9]. Furthermore, the crystallographic polarity of this semiconductor is a key factor in crystal growth and the generation of defects [10]. It has been reported that the properties of this material are a function of various parameters, such as morphology, particle size, and structural defects, which can be modulated with the reaction pH,

temperature, reaction time, heat treatments, and precursors used [11–13].

Unfortunately, the charge carriers in this material have a short lifetimes, due to their high recombination rate, low specific surface area and wide band gap, so 90% of sunlight is not used [14]. Therefore, various strategies have been implemented to expand the range of absorption and reduce these disadvantages, among which incorporation of noble metals [15,16], doping [17,18], and heterojunction creation [19–21]. A heterojunction is an interface between binary or ternary materials with different energy gaps, but one of these materials must absorb visible light [22,23].

On the other hand, ZnSe is a group II-VI semiconductor with a bandgap of 2.7 eV, it has a relatively high refractive index of 2.4 (at room temperature) and is widely used in blue diode lasers and photovoltaic solar cells because of its conduction and valence bands have an adequate positioning for the absorption of solar energy [24,25]. This material has two crystalline phases: wurtzite and zinc blende, with hexagonal and cubic structures, respectively, the structure of zinc blende (sphalerite) is the most stable at room temperature and atmospheric pressure [26]. Furthermore, the positions of its valence and conduction bands allow it to form a staggered heterojunction (type II)

* Corresponding author.

E-mail address: lizethrb@gmail.com (L. Rojas-Blanco).

<https://doi.org/10.1016/j.ceramint.2023.05.009>

Received 11 January 2023; Received in revised form 17 April 2023; Accepted 1 May 2023

Available online 2 May 2023

0272-8842/© 2023 Elsevier Ltd and Techna Group S.r.l. All rights reserved.

with ZnO, thus increasing charge separation [27,28].

The properties of the ZnSe/ZnO heterostructures have been studied for several applications like from solar cells [29,30], CO₂ reduction [31,32], UV photodetector [33], and for the degradation of pollutants by photocatalysis [34–36]. These materials have been obtained by: pulsed laser ablation [37], chemical vapor deposition [38], hydrothermal processes [39], etc. However, most of the methods require complex procedures, high temperatures and long reaction times, which contrasts with the use of renewable sources to produce green energy and avoid damage to the ecosystem. In recent years, microwave-assisted synthesis has attracted attention because dense materials are obtained at lower temperatures and short reaction times. Also, microstructures and nanostructures, coating, functional materials, among others materials can be synthesized [40,41]. Due to the volumetric heating of the reaction solution generated by microwave irradiation, the crystallization process is carried out fast, which causes the generation of imperfections in the crystal structure, such as oxygen vacancies, and a decrease in crystallite size compared to other synthesis processes [42]. This modifies the properties of the material, favoring its photocatalytic performance [43–45].

In the present work, the structural, morphological, and optical properties of the ZnSe/ZnO heterostructures obtained by microwave-assisted synthesis are analyzed, as well as their photocatalytic performance in visible light is analyzed.

2. Experimental details

2.1. Materials

Zinc acetate dihydrate ($\text{Zn}(\text{CH}_3\text{COO})_2 \cdot 2\text{H}_2\text{O}$, 99% Sigma Aldrich), zinc nitrate hexahydrate ($\text{Zn}(\text{NO}_3)_2 \cdot 6\text{H}_2\text{O}$, 99% MEYER), hexamethylenetetramine ($(\text{CH}_2)_6\text{N}_4$, 99% Sigma Aldrich), ascorbic acid ($\text{C}_6\text{H}_8\text{O}_6$, 99% MEYER), sodium selenite (Na_2SeO_3 , 97% MEYER), hydrazine monohydrate ($\text{N}_2\text{H}_4 \cdot \text{H}_2\text{O}$, 98% Sigma Aldrich), ethanol ($\text{C}_2\text{H}_5\text{OH}$, 99.5%, Meyer), acetone ($\text{C}_3\text{H}_6\text{O}$, 99.5%, Baker), methylene blue (MB, $\text{C}_{16}\text{H}_{18}\text{ClN}_3\text{S}$, 98.5% CIVEQ), rhodamine B (RhB, $\text{C}_{28}\text{H}_{31}\text{ClN}_2\text{O}_3$), 4-Nitrophenol (4-NP, $\text{C}_6\text{H}_5\text{NO}_3$, 99% Sigma Aldrich), and deionized water (H_2O). All the reagents used were used without further purification.

The ZnSe/ZnO heterostructures were synthesized in two stages, in the first stage, ZnO was synthesized, which was used as a raw material in phase two, to achieve the synthesis of the heterostructure [46]. A Multiwave PRO microwave reactor from Anton Paar was used throughout the synthesis process.

2.2. Preparation of ZnO particles

For the synthesis of ZnO, two experiments were carried out: in one of them, 0.4 M of $\text{Zn}(\text{CH}_3\text{COO})_2 \cdot 2\text{H}_2\text{O}$ was dissolved in 50 mL of ethanol and 720 μL of deionized water, this solution was kept under constant stirring for 10 min. Subsequently, the solution was placed inside an Anton Paar Multiwave PRO reactor and irradiated at 400 W for 10 min, when the process was finished, the supernatant was removed, and the product obtained was repeatedly washed with water and acetone. Finally, the sample was dried at 80 °C for 12 h, this sample was labeled Z1.

In the other experiment, 8 mM of $\text{Zn}(\text{NO}_3)_2 \cdot 6\text{H}_2\text{O}$, 80 mM of $(\text{CH}_2)_6\text{N}_4$, and 2 mM of $\text{C}_6\text{H}_8\text{O}_6$ were dissolved in a typical synthesis process in 50 mL of H_2O . It was kept under constant stirring for 10 min. Then, it was placed inside an Anton Paar Multiwave PRO reactor at 120 °C for 60 min. Once the process was finished, the supernatant was removed and the product was washed repeatedly with distilled water, to be placed in a drying oven for 12 h at 120 °C. This sample was denoted as Z2. The initial pH values were 5 and 6 for Z1 and Z2, respectively.

2.3. Synthesis of ZnSe/ZnO heterostructures

The heterostructures were synthesized based on the methodology reported by Cho and coworkers [46]. In this stage, 0.1 gr of the previously synthesized ZnO (Z1 and Z2) was used. A solution was prepared with 3.7 mL $\text{N}_2\text{H}_4 \cdot \text{H}_2\text{O}$, 4 mM of Na_2SeO_3 in 50 mL of deionized water. After stirring for 10 min, the reaction mixture was placed into the microwave reactor at 160 °C for 2 min. The heterostructures obtained with Z1 and Z2 were denoted as Z1Se and Z2Se, respectively.

2.4. Characterization

X-ray diffraction (XRD) was performed on a Bruker D2 Phaser diffractometer with Cu-K α radiation ($\lambda = 1.544 \text{ \AA}$) with a passing speed of 4°/minutes. Raman spectra were acquired at room temperature in a HORIBA Xplora PLUS micro-Raman spectrometer with a 532 nm laser source and an acquisition time of 60 s. Morphology was characterized using a FESEM, JEOL InTouch Scope. A transmission electron microscope (JEOL JEM 2200FS and TEM, Hitachi HT7700) was employed to obtain more detailed structural information. The specific surface area was measured in an Autosorb IQ Gas Sorption, before analysis, the samples were degassed at 240 °C for 12 h. UV-Vis absorption spectra were taken with a PerkinElmer Lambda 9 spectrophotometer in the 200–800 nm range. A Thermo Scientific K-Alpha spectrometer was used, with a monochromatic AlKa radiation source (1486 eV) to obtain X-ray photoelectron spectra (XPS). The components of the experimental peaks were obtained using mixed Gaussian-Lorentzian functions, a nonlinear square-fitting algorithm, and Shirley-type background subtraction using XPS peak-fitting software. For the correction of the binding energies (BE) the C1s line at 284.6 eV was used.

2.5. Photocatalyst activity measurement

Methylene blue (MB) (10 ppm), Rhodamine B (RhB) (10 ppm), and 4-Nitrophenol (4-NP) (18 ppm) were used to evaluate the photocatalytic performance of bare ZnO particles and ZnSe/ZnO heterostructures. The working volume was 100 mL of the contaminant solution with 32 mg of catalyst. Before irradiation, this solution was placed in an ultrasonic bath in the dark for 30 min, to achieve adsorption-desorption equilibrium between the contaminating molecules and the surface of the materials evaluated.

Photocatalytic degradation was carried out for 240 min, using a 500W Fully Reflective Solar Simulator (short-arc lamp Xe). The reactor was placed 10 cm below the light source. A UV-Vis spectrophotometer was employed to measure the changes in the absorbance of the analyte. The aliquots were taken every 30 min and centrifuged to separate the solid particles for posterior analysis.

3. Results and discussions

3.1. XRD analysis

Fig. 1-a shows the diffractograms of all the samples. For Z1 and Z2, the data were compared with the JCPDS 36-1451 card, and the characteristic signals of the hexagonal structure of ZnO (wurtzite) are observed, which correspond to planes (100), (002), (101), (102), (110), (103), (200), (112), (201), (004) and (202). In addition to the ZnO peaks, the samples Z1Se and Z2Se, the planes (111), (220), and (311) of the cubic structure of ZnSe (zinc blende) were observed (JCPDS 37-1463).

No additional signals to those of these phases are observed, which corroborates the successful synthesis of the ZnSe/ZnO heterostructure. The average crystallite size was estimated using the Scherrer equation (eq (1)). Moreover, the strain of the ZnO structure, both in the pure particles and in the heterostructures, was calculated through the Uniform Deformation Model (UDM) of the Williamson Hall (W-H) Analysis

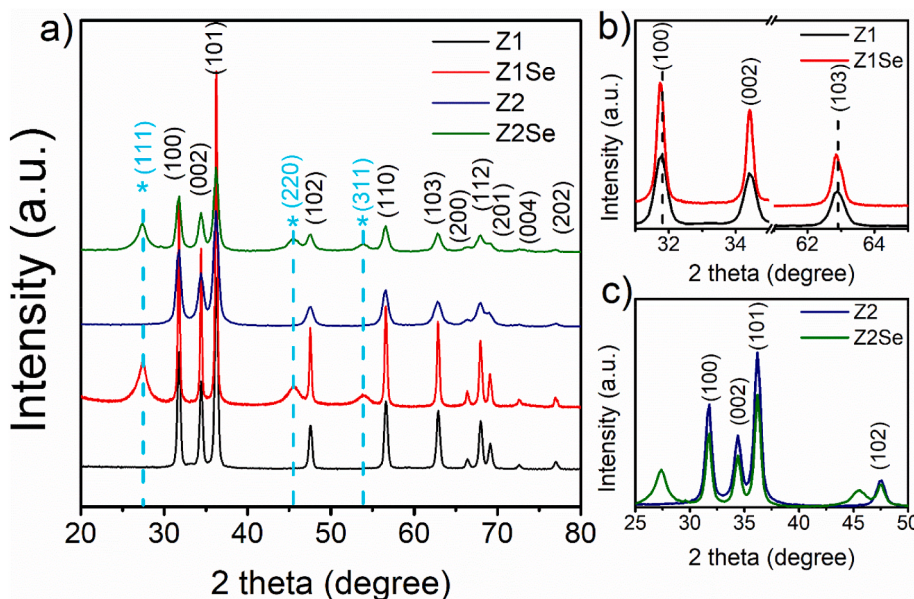


Fig. 1. a) XRD pattern of ZnO particles and ZnSe/ZnO heterostructures, b) Shifts to the left of the planes corresponding to ZnO in Z1Se, and c) decrease in intensity of ZnO peaks in Z2Se.

(eq (2)) [47], the results are summarized in Table 1.

$$D = \frac{K\lambda}{\beta \cos \theta} \quad (1)$$

$$\beta \cos \theta = \frac{K\lambda}{D} + 4\varepsilon \sin \theta \quad (2)$$

Lattice parameters of the ZnO nanocrystals were calculated using the following equations [48]:

$$c = \frac{\lambda}{\sin \theta} \quad (3)$$

$$a = \frac{\lambda}{\sqrt{3} \sin \theta} \quad (4)$$

And to estimate the lattice parameters of the ZnSe nanocrystals, the following equation was used [49]:

$$a = c = \frac{\lambda \sqrt{h^2 + k^2 + l^2}}{2 \sin \theta} \quad (5)$$

Where D is the crystallite size, K is a shape factor (0.9), λ is the X-ray wavelength of radiation $CuK\alpha$ (1.544 Å), β is the width at the mean height of the diffraction peak, θ is the angle of diffraction of the corresponding diffraction peak and ε is the lattice strain.

In the diffractograms of the heterostructures, it was possible to observe slight shifts, both on the left and the right, in the positions of the diffracted peaks corresponding to ZnO, in comparison with the pure ZnO samples. The peaks of the Z1Se sample with more shifts leftward were

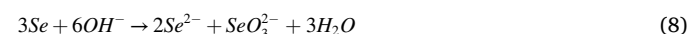
the planes (100) and (103) relative to the position presented in the Z1 sample (Fig. 1-b). Also, the intensity of the ZnO signals becomes less intense when the ZnSe precursor is incorporated into the crystal structure, as can be seen in the planes (100), (002), (101) and (102) of the Z2Se sample (Fig. 1-c).

3.2. Microscopic morphology analysis

In Fig. 2, sample Z1 exhibits semispherical conglomerates with hexagonal facets and an average size of 43 nm, while sample Z2 exhibits spherical agglomerates with an approximate size of 1.18 μm and a porous surface. Although both ZnO particles were synthesized through microwave heating, the different synthesis parameters (precursors, temperature, and reaction time) influenced the morphology of the final product. When the second semiconductor is incorporated, it can be observed in the micrographs that the ZnSe particles are deposited on the surface of the ZnO matrix, so the average size of the Z1Se and Z2Se particles increases to 53 nm and 1.3 μm, respectively. In Fig. 3 the elemental mapping images for Z1Se and Z2Se are presented, which confirm the presence of the elements O, Zn, and Se on the entire surface of the material.

The porous surface observed in the ZnO particles of sample Z2 is attributed to the use of ascorbic acid and hexamethylenetetramine as surfactants in the reaction solution, in addition, the latter acts as a source of OH^- ions. While for obtaining sample Z1 none of these species was used.

For the case of heterostructures, the following formation mechanism has been reported [50,51]:



In the second stage of the synthesis process, the pH value of the reaction mixture was 12, and under these conditions it has been reported that the ZnO surface reacts with the hydroxyl anions, causing a local dissolution

Table 1

XRD estimated structural parameters of the ZnO nanostructures and ZnSe/ZnO heterostructures.

Sample	Av. Crystallite size (nm)	Lattice parameters		Strain	
		a	c		
Z1	ZnO	21	3.2572	5.2173	-0.0007
Z1Se	ZnO	28	3.2579	5.2189	0.0011
	ZnSe	7	5.6415	5.6415	
Z2	ZnO	12	3.2592	5.2277	0.0026
Z2Se	ZnO	14	3.2602	5.2217	0.0022
	ZnSe	5	5.6491	5.6491	

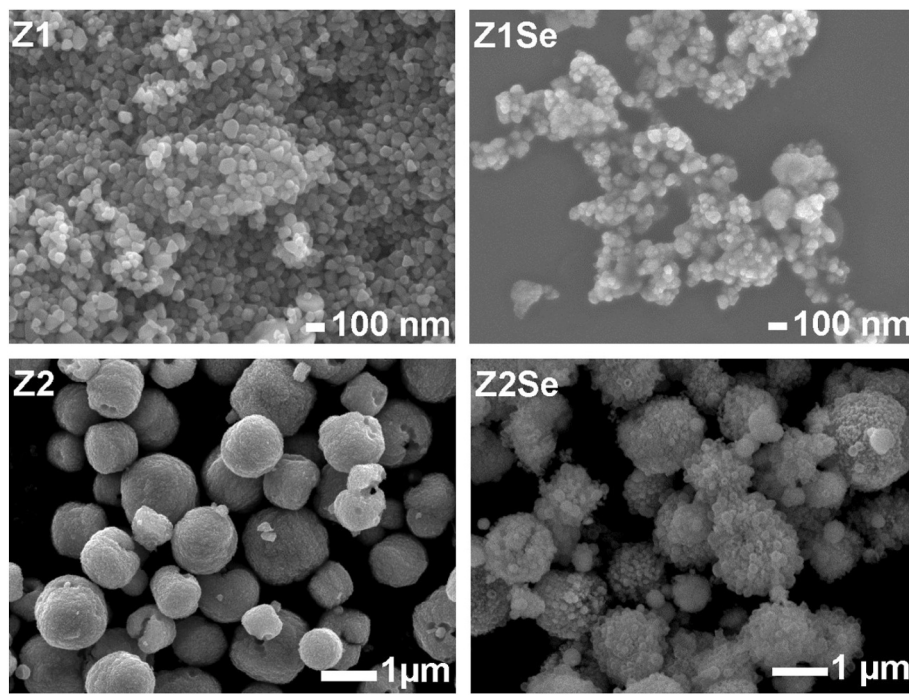


Fig. 2. SEM images of ZnO and ZnSe/ZnO heterostructures.

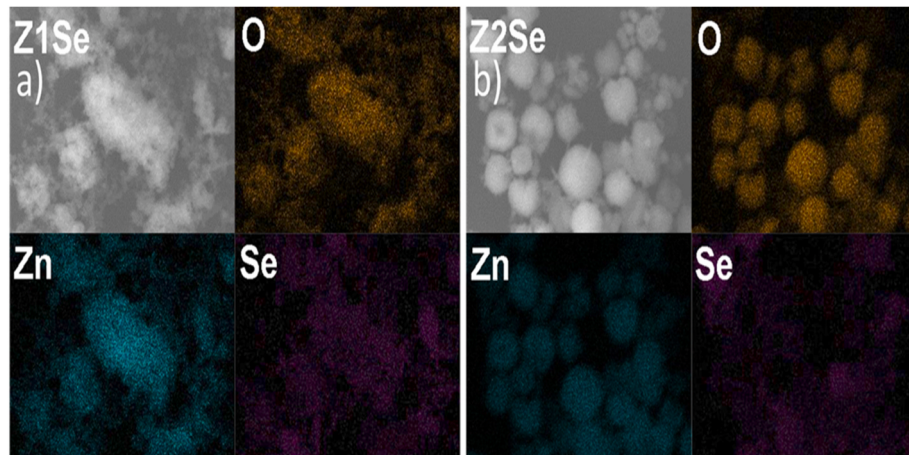


Fig. 3. Elemental mapping of O, Zn and Se of ZnSe/ZnO heterostructures.

of the ZnO allowing the release of $Zn(OH)_4^{2-}$ (eq. (6)). On the other hand, hydrazine reduces SeO_3^{2-} ions to Se^{2-} (eqs. (7) and (8)), which finally react with $Zn(OH)_4^{2-}$ to form ZnSe on the surface of the ZnO particles, which corroborates the observations of the elemental mapping.

Fig. 4 shows TEM images of ZnO and ZnSe/ZnO samples. Particles in Z2 (Fig. 4-d) exhibit ZnO structures less bright than in sample Z1 (Fig. 4-a), which indicates the formation of a denser or more compact structure. The SEM observations are confirmed, where Z1 particles with hexagonal facets and semispherical shapes exhibit a smooth surface, while those of Z2 appear rough.

In Fig. 4-e is possible to observe that ZnSe particles (~140 nm in Z2Se) decorate the ZnO supports. In Fig. 4-c and 4-d the electron diffraction patterns (SAED) of the Z1Se and Z2Se heterostructures, respectively, are presented. The rings and light dots observed reveal the coexistence of polycrystalline and single-crystal structures in these samples. The data were analyzed using the software Process Diffraction, with which the crystalline planes corresponding to the wurtzite phase of

ZnO and the cubic structure of ZnSe could be indexed, corroborating the observations made by XRD.

Therefore, the observed structural and morphological changes can be attributed to the recrystallization process that the ZnO particles undergo in the second synthesis stage since they act with a source of Zn^{2+} ions for the formation of ZnSe/ZnO.

3.3. Raman spectroscopy

Raman spectra of all study samples are shown in Fig. 5. Z1 and Z2 exhibit characteristic signals of the wurtzite structure of ZnO, which are located at 330 cm^{-1} and 438 cm^{-1} , this is attributed to the dispersion processes of multiple phonons ($2E_{2L}$) and the vibrations of the oxygen atoms ($2E_{2H}$), respectively [52,53]. On the other hand, in the case of the ZnSe/ZnO heterostructures (Z1Se and Z2Se), it is possible to observe small shifts in the signals that correspond to ZnO, Sahoo et al. [5] attribute this behavior to the tension generated in the structure of ZnO, attributable to the incorporation of ZnSe into the ZnO matrix. In

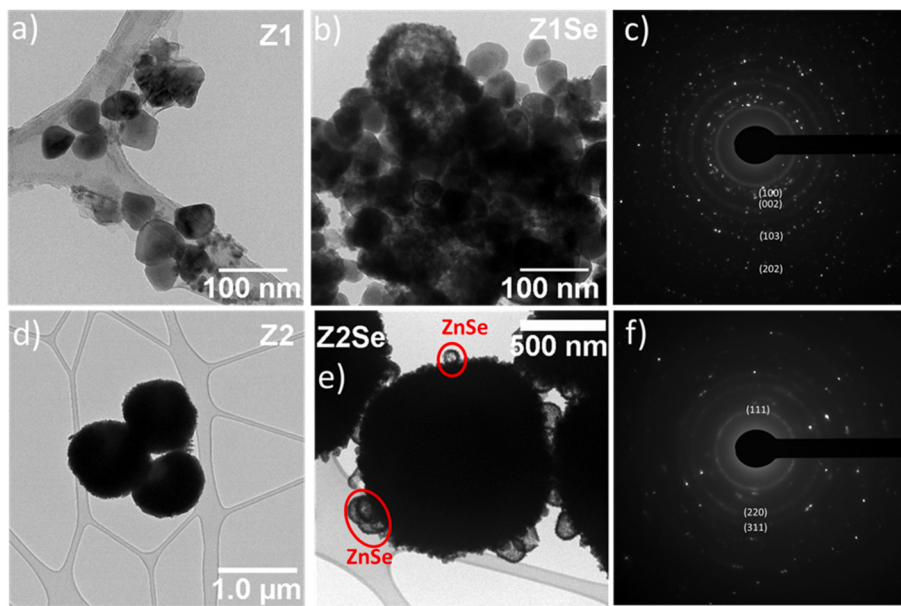


Fig. 4. TEM images of the ZnO structures synthesized under acidic conditions (a–d), ZnSe/ZnO heterostructures (b–e) and, the SAED patterns of Z1Se (c) and Z2Se (f).

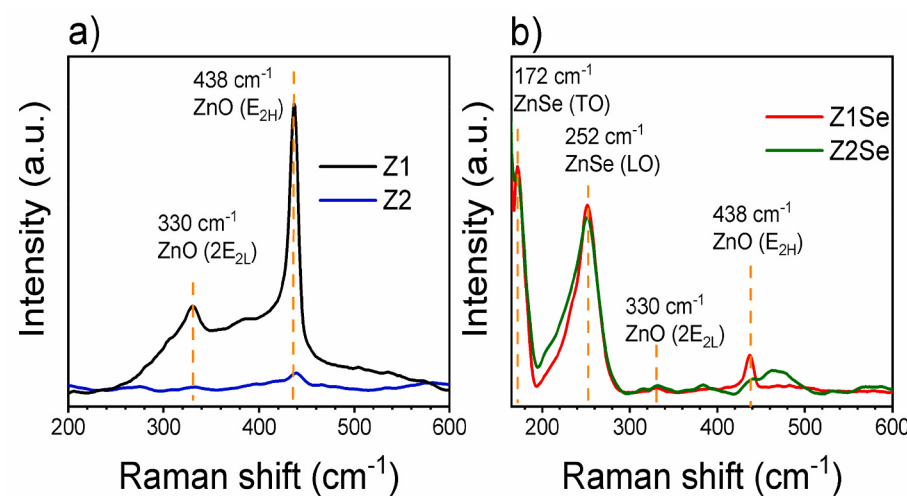


Fig. 5. Room-temperature Raman spectra of a) bare ZnO and b) ZnSe/ZnO heterostructure.

addition, two intense signals occur at $\sim 172\text{ cm}^{-1}$ and 252 cm^{-1} which are associated with the transverse (TO) and longitudinal optical (LO) modes typical of the zinc blende crystal structure of ZnSe [54] that confirmed the formation of the ZnSe/ZnO heterostructure. This corroborates the observations of XRD, where the intensity of the planes associated with ZnO decrease in intensity when ZnSe is incorporated, that is, some surface particles of ZnO serve as sacrificial agents for the formation of the second semiconductor.

3.4. FTIR spectroscopy

To elucidate the existence of organic compounds and inorganic species in the ZnSe/ZnO heterostructures, synthesized using ZnO particles with different properties as support, these samples were characterized by FTIR spectroscopy in the range of $4000\text{--}400\text{ cm}^{-1}$ (Fig. 6).

The band at $\sim 3350\text{ cm}^{-1}$ is associated with $-\text{OH}$ strain vibrations, which can be attributed to water molecules adsorbed on the surface of the material [55], while the band around 430 cm^{-1} corresponds to the frequency of the stretching mode of $\text{Zn}-\text{O}$ corresponding to the

particles used as support for the formation of the heterostructure [56]. Furthermore, the characteristic bending vibration modes of $\text{Zn}-\text{Se}$ are represented by two signals located at 1177 cm^{-1} and 700 cm^{-1} [57]. These signals confirm the formation of the heterostructures since, in their synthesis process, the only source of Zn^{2+} ions in the ZnO particles themselves, undergo a local dissolution process reacting with the Se^{2-} ions, which finally allows the formation of ZnSe as previously mentioned. It is also possible to observe a signal at 900 cm^{-1} corresponding to the $\text{Se}-\text{O}$ stretching, which is related to the internal modes of the group H_2SeO_3 [58], related to the by-products generated in the reaction process.

On the other hand, three signals positioned near 3200 cm^{-1} , $\sim 1600\text{ cm}^{-1}$, and around 1400 cm^{-1} , can be associated with $\text{N}-\text{H}$, $\text{H}-\text{N}-\text{H}$ (antisymmetric bending), and $\text{C}-\text{H}$ bonds, respectively. These indicate that traces of hydrazine are found on the surface of the ZnSe/ZnO heterostructures [57,59], which is possible because no sample was subjected to any heat treatment. It is also important to point out that the presence of these species could affect the interaction of both the contaminating molecules and the water with the surface of the

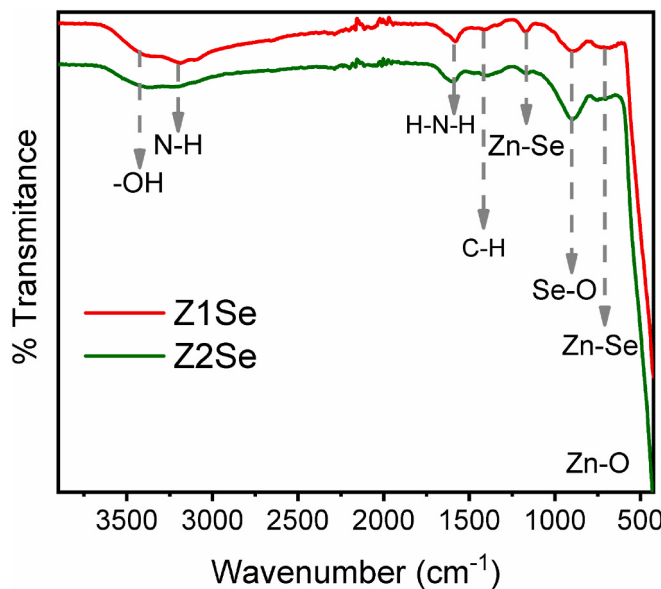


Fig. 6. FTIR spectra at room temperature of the ZnSe/ZnO heterostructures with different sources of Zn^{2+} ions.

photocatalyst in the photocatalysis process [60,61].

3.5. UV-Vis Spectroscopy

UV-Vis absorption spectra for the ZnO particles and the ZnSe/ZnO heterostructures are presented in Fig. 7. Samples Z1 and Z2 show a characteristic absorption edge of ZnO, which is around 360 nm, while samples Z1Se and Z2Se show absorption signals in both the UV and visible regions. In the heterostructures, two bands can be seen around 420 and 520 nm which are attributed to the absorption of the ZnSe particles on the surface of the ZnO structures. Some investigations attribute that the band located around 420 nm is associated with the formation of ZnSe in the wurtzite phase at the interface of ZnO and cubic ZnSe [62].

Tauc equation was used to calculate the forbidden gap values for each of the samples:

$$\alpha h\nu = A(h\nu - E_g)^n \quad (10)$$

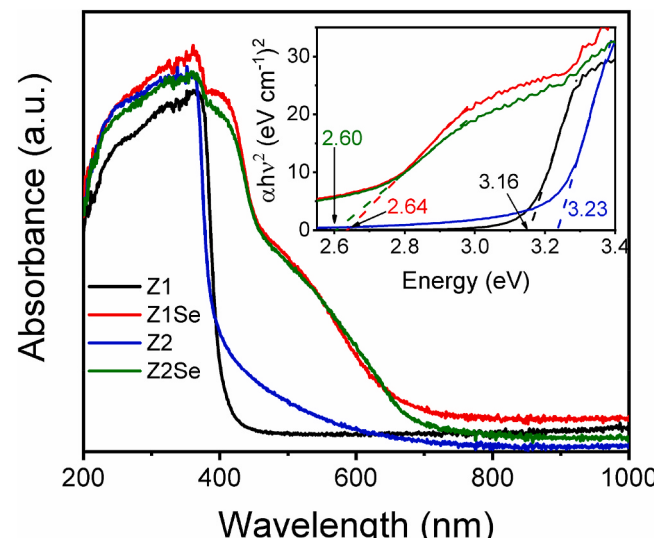


Fig. 7. UV-Vis absorption spectra and (inset) bandgap measurement of ZnO particles and ZnSe/ZnO heterostructures.

Where α is the adsorption coefficient, A is a constant, and $n = \frac{1}{2}$ for direct transition semiconductors [63]. Through a linear fit of the graphs of $(\alpha h\nu)^2$ vs $(h\nu)$ (inset Fig. 6), the values of E_g were calculated. Z1 presented an energy gap of 3.16 eV, while for Z2 it was 3.23 eV. Another hand, the Z1Se and Z2Se heterostructures exhibited a bandgap of 2.64 and 2.60 eV, respectively. This decrease in the values of the energy gap is related to the improvement in the absorption of the heterostructures compared to the pure ZnO particles, also, the values obtained are congruent with those reported in the literature [64].

The samples Z1Se and Z1 exhibit higher absorption for wavelengths greater than 800 nm, this behavior can be associated with the existence of O vacancies, generated by the rapid crystallization process, which can increase the photocatalytic performance of the materials [65,66].

3.6. X-ray photoelectron spectroscopy

The chemical composition of the samples was confirmed by X-ray photoelectron spectroscopy (XPS). General XPS spectra for Z1, Z2, Z1Se, and Z2Se are shown in Fig. 8. It is possible to observe an inset in all the plots, which corresponds to each sample's atomic content (%). In Samples Z1 (a) and Z2 (c), it is evident the absence of Se, is present in Z1Se (b) and Z2Se (d).

Fig. 9 corresponds to XPS spectra at the core level and demonstrates the formation of binding Zn-Se in samples Z1Se and Z2Se. Fig. 9-a and 9-b show Zn 2p spectra; the plots show a doublet at ~ 1021 and ~ 1044 eV, corresponding to the Zn 2p_{3/2} and Zn 2p_{1/2} lines, respectively.

The difference between the two binding energies (~ 23 eV) suggests a +2 oxidation state for Zn [67], suggesting the presence of ZnO, according to the literature [68]. The Zn 2p peaks were resolved into two peaks: Table 2 lists the two components for each sample (Z1Se and Z2Se); furthermore, it provides information about the position, area, and FWHM, for each specie identified. Finding ZnO specie, centered at 1021.3 and 1021.4, validates the presence of ZnO [69]. Peaks centered at 1023.1 (Z1Se) and 1022.1 (Z2Se) correspond to the formation of ZnSe particles [70], and the difference in positions is due to the concentration of Se, which is less in Z2Se, this affirmation is agree with the literature [71].

3.7. Textural analysis

Textural properties were investigated by nitrogen physisorption, the adsorption-desorption isotherms are presented in Fig. 10. BET multi-point method was used to estimate the specific surface area and the pore size distribution in the samples was obtained using the BJH (Barret, Joyner, Halenda) method on the adsorption isotherm. Z1 presented an area_{BET} of 9.95 m²/g this increased to 23.41 m²/g when the ZnSe particles were incorporated (Z1Se), however, the pore size in heterostructure Z1Se presented a reduction of 55% in comparison with the pores of Z1. This behavior indicates that the ZnSe particles not only grew on the surface but have also deposited onto the pores of the support (Z1), which is consistent with the change in the hysteresis loop observed in the figure.

On the other hand, sample Z2 exhibited an area_{BET} of 10.62 m²/g while in the Z2Se heterostructure, this area practically doubled. As can be seen, the shape of the hysteresis loop is maintained constant in Z2 and Z2Se, which indicates that the structure of the pores in both samples is similar, also the pore size was maintained at 1.57 nm. The pore size distribution for each of the samples is shown in the insets in Fig. 10.

This significant increase in the specific surface area in the ZnSe/ZnO heterostructures, together with its improved absorption in the visible region, could improve the performance of these materials in photocatalytic applications.

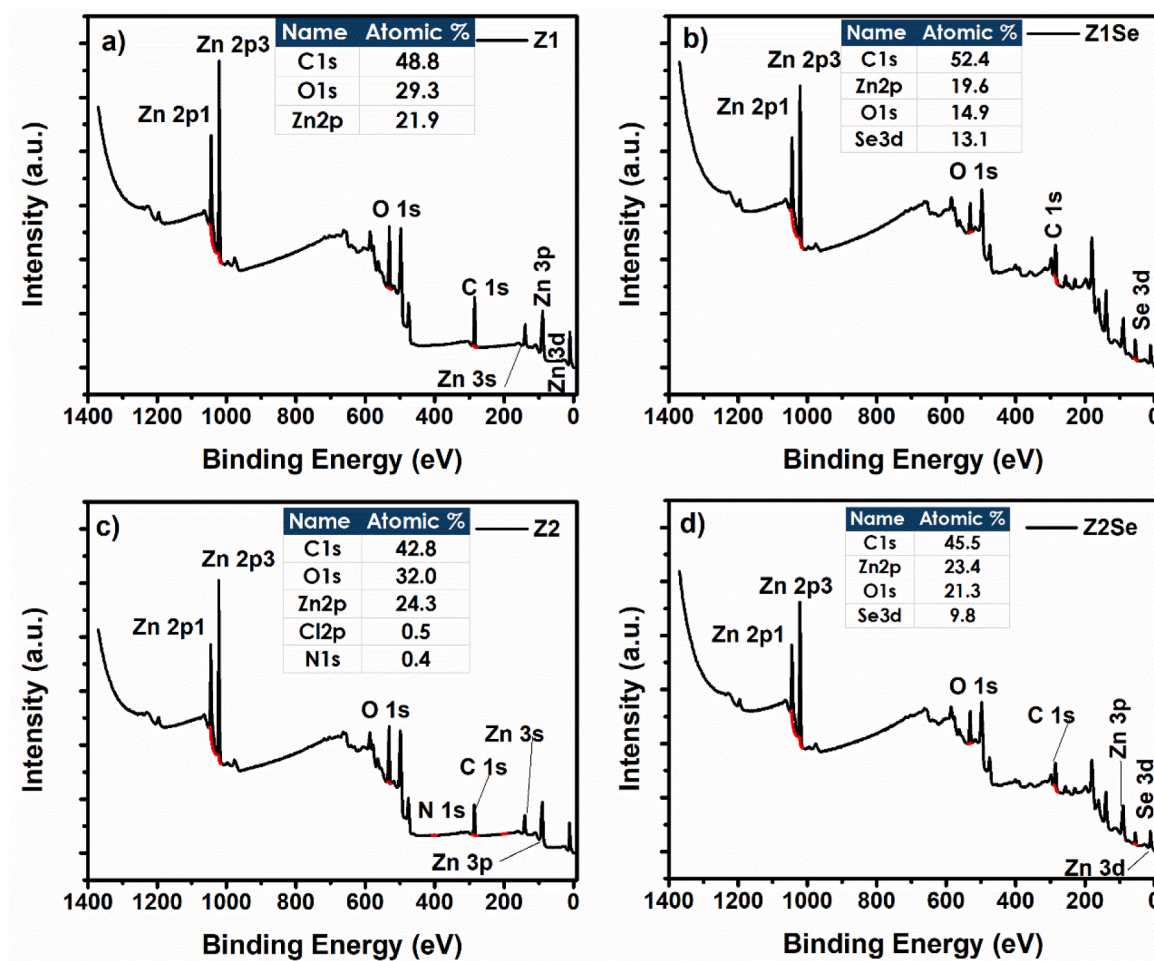


Fig. 8. a) General XPS spectra and high-resolution core level spectra of b) O 1s, c) Zn 2p and d) Se 3d of ZnO particles and ZnSe/ZnO heterostructures.

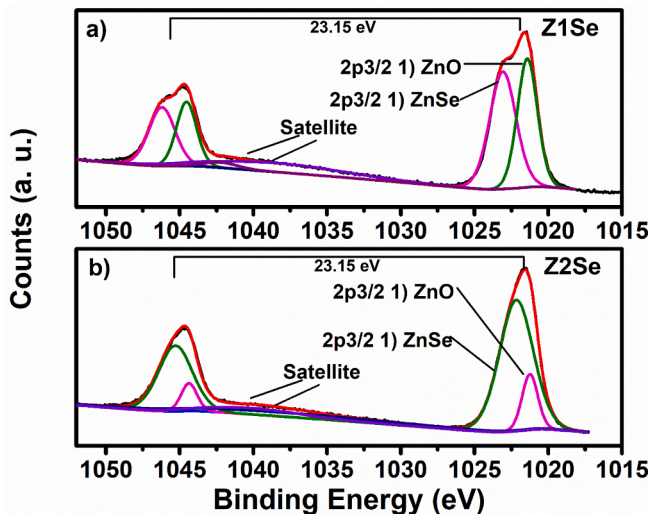


Fig. 9. XPS core level spectra of Zn 2p a) Z1Se and b) Z2Se.

3.8. Photocatalytic activity

In Fig. 11 the absorbance spectra for a-b) MB and d-e) Rh B is presented. Samples Z1Se and Z2Se were the ones that achieved the best photocatalytic performance for bare ZnO particles. This is corroborated

Table 2
Species assigned for Z1Se and Z2Se samples.

Z1Se				
Specie	Position (eV)	Area	FWHM (eV)	%GL (%)
ZnO	1021.4	15338.9	1.6	30
ZnSe	1023.1	18395.1	2.1	30
Satellite	1038.4	4888.7	10.9	30
Satellite	1042.2	733.6	2.7	30
Z2Se				
Specie	Position (eV)	Area	FWHM (eV)	%GL (%)
ZnO	1021.3	5810.4	1.2	30
ZnSe	1022.1	29176.1	2.7	30
Satellite	1038.2	4592.8	18.6	30
Satellite	1040.1	2624.8	7.6	30

by the $\text{de} (\text{C}/\text{C}_0)$ vs time graphs (Fig. 11-c, 11-f). For MB, the degradation efficiency after 240 min of irradiation was as follows: Z1Se (45%) > Z1 (9%) > Z2Se (6%) > Z2 (1%). While for RhB, it was: Z1Se (73%) > Z2Se (14%) > Z1 (11%) > Z2 (7%). In these graphs, it can be seen that, in the process of photolysis of both dyes, they remain stable, so the degradation percentages achieved can be attributed to the photocatalysts used.

In addition to these dyes, the photocatalytic performance of the synthesized materials was analyzed against 4-Nitrophenol (4-NP) (18 ppm). Fig. 11-g shows the absorption spectra of the photolysis test performed on this contaminant. When starting the irradiation process, the original spectrum is modified, and a small signal appears located at

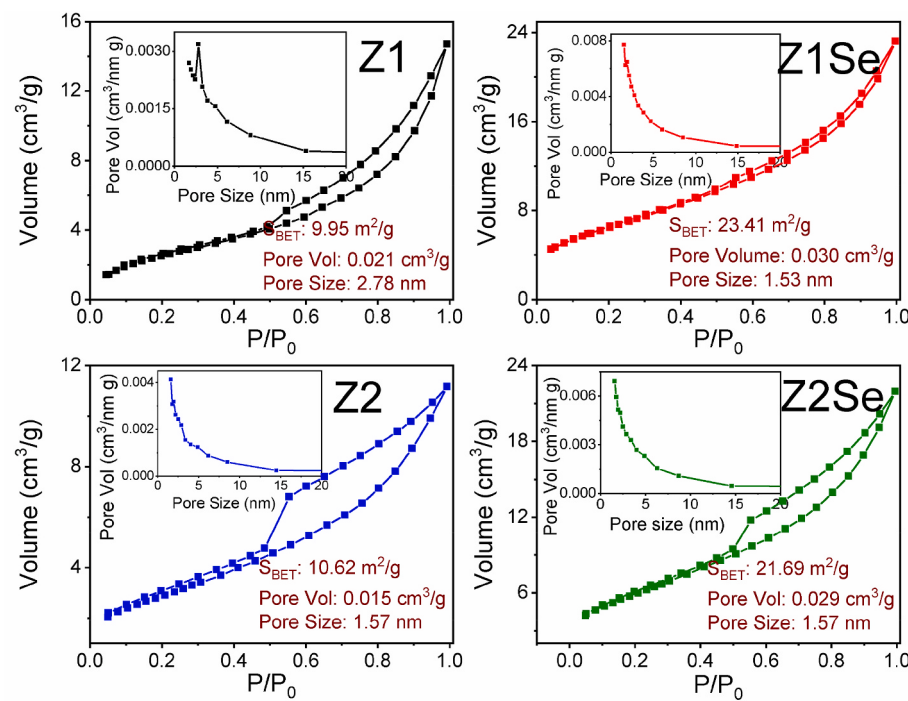


Fig. 10. N₂ adsorption-desorption isotherms and (insets)pore size distribution of ZnO particles (Z1 and Z2) and ZnSe/ZnO heterostructures (Z1Se and Z2Se) synthezized by microwave irradiation.

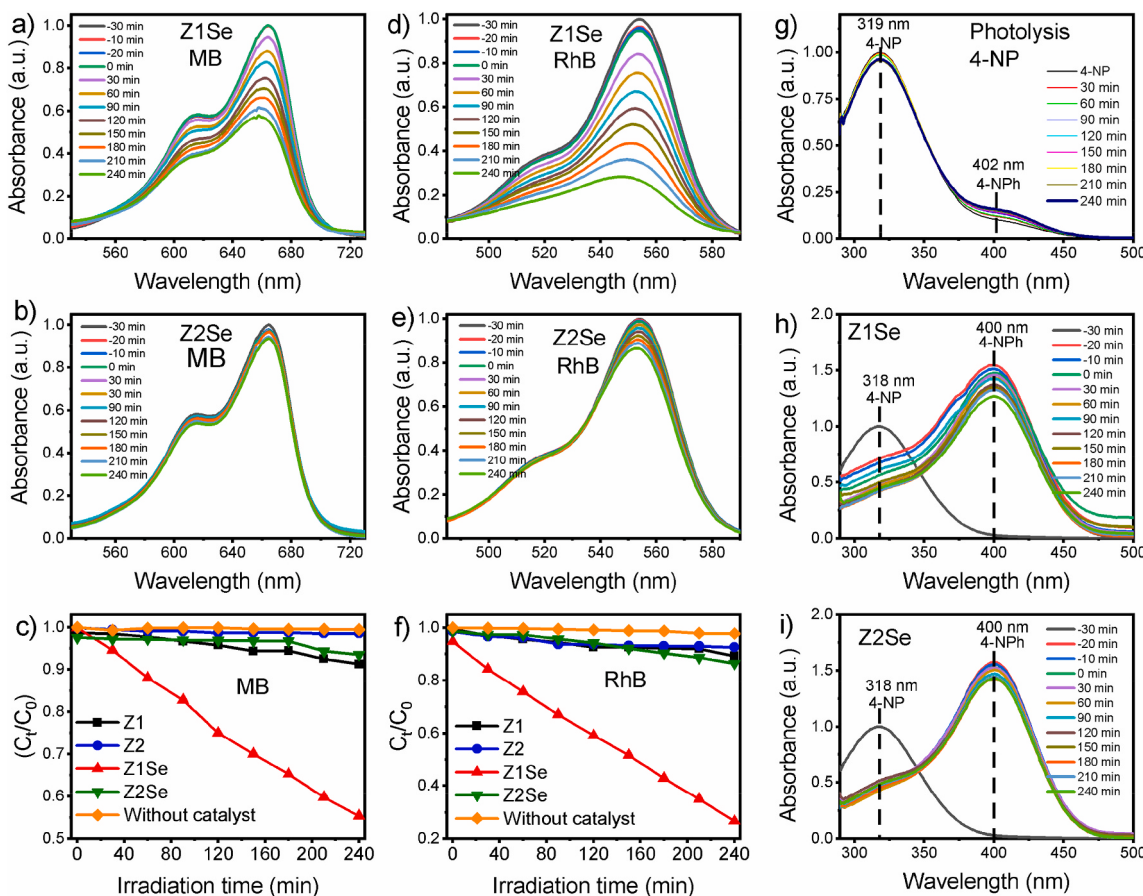


Fig. 11. Absorbance spectra of MB (a-b) and RhB (d-e). C vs t plots of the dyes evaluated, using ZnO and ZnSe/ZnO as photocatalysts (c and f). 4-NP absorbance spectra in g) photolysis test, h-i) photocatalytic evaluation using ZnSe/ZnO heterostructures.

402 nm, which is related to the phenolate ion (4-NPh) [72], which indicates that the energy emitted by the simulator Solar energy is capable of inducing changes in the original pollutant molecule.

In the adsorption-desorption stage, the color of the solution changed from semi-transparent to slightly yellow. These changes occurred with each of the photocatalysts evaluated, and an intense signal corresponding to the 4-NPh ion appeared in the absorbance spectrum. When the photocatalytic process starts, the intensity of this signal decreases slightly, which could indicate that the photocatalysts used to promote the decomposition of this pollutant, however, their performance is not optimal. The absence of sodium borohydride, sodium sulfite, or other reactive agents that have been reported for photoassisted chemical reduction of 4NP is probably related to the observed behavior [73,74]. In Fig. 11-h, Fig-i, it is possible to observe isosbestic points, around 330–350 nm, indicating that both species (4-NP and 4NPh) are present in the solution [75]. In this case, the Z1Se and Z2Se samples showed a greater decrease in the 4-NPN band than the other two study samples.

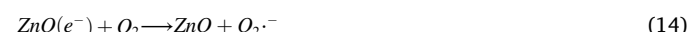
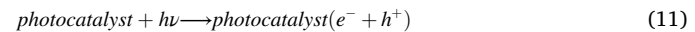
To estimate the degradation percentage of this contaminant, the band located at 402 nm was used, despite being the 4-NPh band. This is an existing form of 4-NP, so the reduction of 4-NPh is equivalent to the reduction of 4-NP [76]. Its photocatalytic efficiency was as follows: Z1Se (20%) > Z1(18%) > Z2Se (9%) > Z2 (1%).

The improved photocatalytic performance of the heterostructures in relation to their respective supports, that is, the pure ZnO particles, is related to multiple factors, such as greater absorption of visible light due to the incorporation of the ZnSe particles, greater specific surface area, which contributes to a greater number of species being in contact with the photocatalyst, giving way to redox reactions that favor the photocatalytic process and, finally, to the heterojunction formed in the ZnSe/ZnO heterostructure, since it prolongs the lifetime of the charge carriers. Flores et al. [77] indicate that the carriers are spatially separated under indirect transition from the ZnSe valence band to the ZnO conduction band at the interface, decreasing the recombination rate of the pair e^-/h^+ pair.

Fig. 12 shows the schemes of the band positions of ZnO and ZnSe before and after the formation of the type II heterojunction (staggered) [78]. When the heterostructure has been formed in these materials, different mechanisms promote charge separation: i) the photogenerated holes in the ZnO valence band can migrate to the ZnSe valence band (energetically possible due to the type II alignment) [64] and ii) the electric field generated at the ZnO-ZnSe junction interface provides a direct driving force for the efficient separation of photogenerated charges [79], iii) electrons in the conduction band of ZnO can be transferred to both the ZnSe conduction band and the ZnSe valence band at the interface [79,80].

Ehsan [81] proposed a possible photocatalytic mechanism for the

"ZnSe/ZnO" heterostructures, which is described by the following equations



4. Conclusions

Through the microwave-assisted hydrothermal method, it was possible to obtain ZnSe/ZnO heterostructures. The DRX, Raman, and XPS results confirm the presence of ZnSe particles in the material. The incorporation of ZnSe in the matrix of ZnO generated that the heterostructures will increase the absorption in the visible region. In addition, the grain size in the heterostructures increased between 12 and 24% compared to those presented by the pure ZnO particles, the results confirm that the ZnSe was not only generated on the surface of the ZnO but also in its pores. ZnSe/ZnO heterostructures exhibit a nearly 100% increase in specific surface area.

In general, the ZnSe/ZnO heterostructures presented higher efficiency than the ZnO particles, due to the synergy of the optical, structural and optical properties that reduced charge recombination. However, the presence of traces of by-products of the reaction process, in addition to promoting conglomerates in the photocatalysts, could intervene in the photocatalysis process, preventing better yields.

Declaration of competing interest

The authors declare that they have no known competing financial

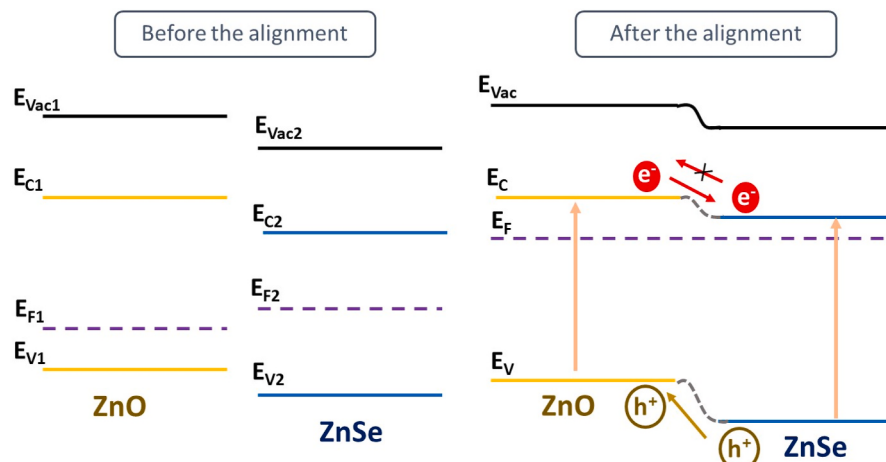


Fig. 12. Illustrations of the positions of the energy bands of ZnO and ZnSe before and after the alignment (type II heterojunction) [78].

interests or personal relationships that could have appeared to influence the work reported in this paper.

Acknowledgements

Arellano-Cortaza thanks the “Estancias Posdoctorales por Mexico” program for the grant.

References

- [1] L. Zhou, T. Yang, Z. Fang, J. Zhou, Y. Zheng, C. Guo, L. Zhu, E. Wang, X. Hou, K.-C. Chou, Z.L. Wang, Boosting of water splitting using the chemical energy simultaneously harvested from light, kinetic energy and electrical energy using N-doped 4H-SiC nanohole arrays, *Nano Energy* 104 (2022), 107876, <https://doi.org/10.1016/j.nanoen.2022.107876>.
- [2] S. Rajendran, M.M. Khan, F. Gracia, J. Qin, V.K. Gupta, S. Arumainathan, Ce³⁺-ion-induced visible-light photocatalytic degradation and electrochemical activity of ZnO/CeO₂ nanocomposite, *Sci. Rep.* 6 (2016), 31641, <https://doi.org/10.1038/srep31641>.
- [3] T. Yang, Q. Li, X. Chang, K.-C. Chou, X. Hou, Preparation of TiO_xNy/TiN composites for photocatalytic hydrogen evolution under visible light, *Phys. Chem. Chem. Phys.* 17 (2015) 28782–28788, <https://doi.org/10.1039/C5CP04768D>.
- [4] M.C. Ariza-Tarazona, J.F. Villarreal-Chiu, J.M. Hernández-López, J. Rivera De la Rosa, V. Barbieri, C. Siligardi, E.I. Cedillo-González, Microplastic pollution reduction by a carbon and nitrogen-doped TiO₂: effect of pH and temperature in the photocatalytic degradation process, *J. Hazard Mater.* 395 (2020), 122632, <https://doi.org/10.1016/j.jhazmat.2020.122632>.
- [5] S. Mondal, M.E. De Andra Reyes, U. Pal, Plasmon induced enhanced photocatalytic activity of gold loaded hydroxyapatite nanoparticles for methylene blue degradation under visible light, *RSC Adv.* 7 (2017) 8633–8645, <https://doi.org/10.1039/C6RA28640B>.
- [6] M. Santos-Beltrán, F. Paraguay-Delgado, R. García, W. Antúnez-Flores, C. Ornelas-Gutiérrez, A. Santos-Beltrán, Fast methylene blue removal by MoO₃ nanoparticles, *J. Mater. Sci. Mater. Electron.* 28 (2017) 2935–2948, <https://doi.org/10.1007/s10854-016-5878-2>.
- [7] D.S. Paeng, B.T. Huy, N.T.K. Phuong, V.D. Dao, Y.I. Lee, Photocatalytic activity of Yb, Er, Ce-codoped TiO₂ for degradation of Rhodamine B and 4-chlorophenol, *J. Chem. Technol. Biotechnol.* 95 (2020) 2664–2673, <https://doi.org/10.1002/jctb.6292>.
- [8] A. Bedia, F.Z. Bedia, M. Aillerie, N. Maloufi, B. Benyoucef, Morphological and optical properties of ZnO thin films prepared by spray pyrolysis on glass substrates at various temperatures for integration in solar cell, *Energy Proc.* 74 (2015) 529–538.
- [9] N. Matinise, X.G. Fuku, K. Kaviyarasu, N. Mayedwa, M. Maaza, ZnO nanoparticles via Moringa oleifera green synthesis: physical properties & mechanism of formation, *Appl. Surf. Sci.* 406 (2017) 339–347.
- [10] G. Pérez-Hernández, A. Vega-Poot, I. Pérez-Juárez, J.M. Camacho, O. Arés, V. Rejón, J.L. Peña, G. Oskam, Effect of a compact ZnO interlayer on the performance of ZnO-based dye-sensitized solar cells, *Sol. Energy Mater. Sol. Cell.* 100 (2012) 21–26, <https://doi.org/10.1016/j.solmat.2011.05.012>.
- [11] S. Music, A. Saric, S. Popovic, Dependence of the microstructural properties of ZnO particles on their synthesis, *J. Alloys Compd.* 448 (2008) 277–283, <https://doi.org/10.1016/j.jallcom.2006.10.021>.
- [12] Z. Ait Abdellouhab, D. Djouadi, A. Chelouche, L. Hammiche, T. Touam, Structural and morphological characterizations of pure and Ce-doped ZnO nanorods hydrothermally synthesized with different caustic bases, *Materials Science- Poland* 38 (2020) 228–235, <https://doi.org/10.2478/msp-2020-0038>.
- [13] E.K. Droeppen, B.S. Wee, S.P. Chin, K.Y. Kok, E.A. Asare, Synthesis and Characterization of Single Phase ZnO Nanostructures via Solvothermal Method: Influence of Alkaline Source, 2019.
- [14] D. Das, P. Nandi, Synthesis of CdS/GO modified ZnO heterostructure for visible light dye degradation applications, *Appl. Surf. Sci.* 570 (2021), 151260.
- [15] R.M. Mohamed, I.A. Mkhald, M. Alhaddad, A. Basaleh, K.A. Alzahrani, A.A. Ismail, Enhanced CO₂ photocatalytic conversion into CH₃OH over visible-light-driven Pt nanoparticle-decorated mesoporous ZnO-ZnS S-scheme heterostructures, *Ceram. Int.* 47 (2021) 26779–26788, <https://doi.org/10.1016/j.ceramint.2021.06.086>.
- [16] L. Muñoz-Fernandez, A. Sierra-Fernandez, O. Milošević, M.E. Rabanal, Solvothermal synthesis of Ag/ZnO and Pt/ZnO nanocomposites and comparison of their photocatalytic behaviors on dyes degradation, *Adv. Powder Technol.* 27 (2016) 983–993, <https://doi.org/10.1016/j.apnt.2016.03.021>.
- [17] P. Dumrongrojathanath, A. Phuruangrat, S. Thongtem, T. Thongtem, Photocatalysis of Cd-doped ZnO synthesized with precipitation method, *Rare Met.* 40 (2021) 537–546, <https://doi.org/10.1007/s12598-019-01283-6>.
- [18] S. Sa-nguanprang, A. Phuruangrat, T. Thongtem, S. Thongtem, Synthesis, analysis, and photocatalysis of Mg-doped ZnO nanoparticles, *Russ. J. Inorg. Chem.* 64 (2019) 1841–1848, <https://doi.org/10.1134/S0036023619140158>.
- [19] B. Tian, R. Dong, J. Zhang, S. Bao, F. Yang, J. Zhang, Sandwich-structured AgCl@Ag@TiO₂ with excellent visible-light photocatalytic activity for organic pollutant degradation and E. coli K12 inactivation, *Appl. Catal., B* 158–159 (2014) 76–84, <https://doi.org/10.1016/J.APCATB.2014.04.008>.
- [20] A. Das, M. Patra, M. Kumar P, M. Bhagavathiachari, R.G. Nair, Role of type II heterojunction in ZnO-In₂O₃ nanodisks for enhanced visible-light photocatalysis through the synergy of effective charge carrier separation and charge transport, *Mater. Chem. Phys.* 263 (2021), 124431, <https://doi.org/10.1016/j.matchemphys.2021.124431>.
- [21] Y. Min, K. Zhang, Y. Chen, Y. Zhang, W. Zhao, Synthesis of nanostructured ZnO/B₂WO₆ heterojunction for photocatalysis application, *Sep. Purif. Technol.* 92 (2012) 115–120, <https://doi.org/10.1016/j.seppur.2012.03.012>.
- [22] B.J. Skromme, G.K. Sujan, Semiconductor heterojunctions *, Reference Module in Materials Science and Materials Engineering (2018) 1–13, <https://doi.org/10.1016/B978-0-12-803581-8.11219-6>.
- [23] Y. Zheng, X. Hou, Q. Li, Z. Fang, T. Yang, T. Liang, X. Duan, M. Shang, W. Yang, Electrostatic interaction assisted synthesis of a CdS/BCN heterostructure with enhanced photocatalytic effects, *J Mater Chem C Mater* 8 (2020) 1803–1810, <https://doi.org/10.1039/C9TC05896F>.
- [24] Q. Peng, Y. Dong, Y. Li, ZnSe semiconductor hollow microspheres, *Angew. Chem. Int. Ed.* 42 (2003) 3027–3030, <https://doi.org/10.1002/anie.200250695>.
- [25] E. Liu, X. Zhang, P. Xue, J. Fan, X. Hu, Carbon membrane bridged ZnSe and TiO₂ nanotube arrays: fabrication and promising application in photoelectrochemical water splitting, *Int. J. Hydrogen Energy* 45 (2020) 9635–9647, <https://doi.org/10.1016/j.ijhydene.2020.01.207>.
- [26] Z. Shi, J. Liu, D. Liu, Q. Zhang, J. Lang, X. Li, Preparation and comparison of the photocatalytic properties of ZnSe with different crystalline phases, *Phys. Status Solidi B* 256 (2019) 1–7, <https://doi.org/10.1002/pssb.201800754>.
- [27] A. Gołębiewska, M.P. Kobylański, A. Zaleska-Medynska, Fundamentals of metal oxide-based photocatalysis, <https://doi.org/10.1016/B978-0-12-811634-0.00002-0>, 2018.
- [28] I.J. Ani, U.G. Akpan, M.A. Olutoye, B.H. Hameed, Photocatalytic degradation of pollutants in petroleum refinery wastewater by TiO₂ and ZnO-based photocatalysts: recent development, *J. Clean. Prod.* 205 (2018) 930–954, <https://doi.org/10.1016/j.jclepro.2018.08.189>.
- [29] Z. Wu, W. Wang, Y. Cao, J. He, Q. Luo, W.A. Bhutto, S. Li, J. Kang, A beyond near-infrared response in a wide-bandgap ZnO/ZnSe coaxial nanowire solar cell by pseudomorphic layers, *J Mater Chem A Mater* 2 (2014) 14571–14576, <https://doi.org/10.1039/c4ta02971b>.
- [30] Q. Luo, Z. Wu, J. He, Y. Cao, W.A. Bhutto, W. Wang, X. Zheng, S. Li, S. Lin, L. Kong, J. Kang, Facile synthesis of composition-tuned ZnO/ZnxCd_{1-x}Se nanowires for photovoltaic applications, *Nanoscale Res. Lett.* 10 (2015), <https://doi.org/10.1186/s11671-015-0886-3>.
- [31] C. Cai, Y.F. Xu, H.Y. Chen, X.D. Wang, D. bin Kuang, Porous ZnO@ZnSe nanosheet array for photoelectrochemical reduction of CO₂, *Electrochim. Acta* 274 (2018) 298–305, <https://doi.org/10.1016/j.electacta.2018.04.108>.
- [32] S. Zhang, X. Yin, Y. Zheng, Enhanced photocatalytic reduction of CO₂to methanol by ZnO nanoparticles deposited on ZnSe nanosheet, *Chem. Phys. Lett.* 693 (2018) 170–175, <https://doi.org/10.1016/j.cplett.2018.01.018>.
- [33] S. Park, S. Kim, G.J. Sun, D.B. Byeon, S.K. Hyun, W.I. Lee, C. Lee, ZnO-core/ZnSe-shell nanowire UV photodetector, *J. Alloys Compd.* 658 (2016) 459–464, <https://doi.org/10.1016/j.jallcom.2015.10.247>.
- [34] G. Xu, Z. Zhang, T. Li, M. Du, Y. Guan, C. Guo, Continuous high-efficient degradation of organic pollutants based on sea urchin-like Fe₃O₄/ZnO/ZnSe heterostructures in photocatalytic magnetically fixed bed reactor, *Colloids Surf. A Physicochem. Eng. Asp.* 603 (2020), 125198, <https://doi.org/10.1016/j.colsurfa.2020.125198>.
- [35] A.M. Mostafa, A.A. Menazea, Laser-assisted for preparation ZnO/CdO thin film prepared by pulsed laser deposition for catalytic degradation, *Radiat. Phys. Chem.* 176 (2020), 109020, <https://doi.org/10.1016/j.radphyschem.2020.109020>.
- [36] S. Cho, J.-W. Jang, J. Kim, J.S. Lee, W. Choi, K.-H. Lee, Three-Dimensional type II ZnO/ZnSe heterostructures and their visible light photocatalytic activities, *Langmuir* 27 (2011) 10243–10250, <https://doi.org/10.1021/la201755w>.
- [37] N. Al Abass, T.F. Qahtan, M.A. Gondal, R.A. Moqbel, A. Bubshait, Laser-assisted synthesis of ZnO/ZnSe hybrid nanostructured films for enhanced solar-light induced water splitting and water decontamination, *Int. J. Hydrogen Energy* 45 (2020) 22938–22949, <https://doi.org/10.1016/j.ijhydene.2020.06.193>.
- [38] J. He, W. Wang, X. Zheng, Y. Cao, L. Kong, Y. Wu, Z. Wu, J. Kang, Enhanced photocatalytic efficiency of ZnO/ZnSe coaxial nanowires through interfacial strain modification, *Physica E Low Dimens Syst Nanostruct* 103 (2018) 430–434, <https://doi.org/10.1016/j.physe.2018.06.029>.
- [39] H. Liu, Y. Hu, X. He, H. Jia, X. Liu, B. Xu, In-situ anion exchange fabrication of porous ZnO/ZnSe heterostructural microspheres with enhanced visible light photocatalytic activity, *J. Alloys Compd.* 650 (2015) 633–640, <https://doi.org/10.1016/J.JALLCOM.2015.08.001>.
- [40] I. Bilecka, M. Niederberger, Microwave chemistry for inorganic nanomaterials synthesis, *Nanoscale* 2 (2010) 1358–1374, <https://doi.org/10.1039/b9nr00377k>.
- [41] M. Baghbanzadeh, L. Carbone, P.D. Cozzoli, C.O. Kappe, Microwave-assisted synthesis of colloidal inorganic nanocrystals, *Angew. Chem. Int. Ed.* 50 (2011) 11312–11359, <https://doi.org/10.1002/anie.201101274>.
- [42] W. Klich, M. Inada, H. Gao, H. Saito, M. Ohtaki, Microwave synthesis of ZnO microcrystals with novel asymmetric morphology, *Adv. Powder Technol.* 32 (2021) 4356–4363, <https://doi.org/10.1016/j.ap.2021.09.038>.
- [43] P. Rodionovs, J. Grabis, Photocatalytic activity of Eu₂O₃/ZnO and Sm₂O₃/ZnO prepared by microwave-assisted hydrothermal method, in: NANOCON Conference Proceedings - International Conference on Nanomaterials, TANGER Ltd., 2020, pp. 163–168, <https://doi.org/10.37904/nanocon.2019.8562>.
- [44] S. Choudhary, A. Bisht, S. Mohapatra, Microwave-assisted synthesis of alpha-Fe₂O₃/ZnFe₂O₄/ZnO ternary hybrid nanostructures for photocatalytic applications, *Ceram. Int.* 47 (2021) 3833–3841, <https://doi.org/10.1016/j.ceramint.2020.09.243>.
- [45] A. Phuruangrat, S. Siri, P. Waduba, S. Thongtem, T. Thongtem, Microwave-assisted synthesis, photocatalysis and antibacterial activity of Ag nanoparticles supported

- on ZnO flowers, *J. Phys. Chem. Solid.* 126 (2019) 170–177, <https://doi.org/10.1016/j.jpcs.2018.11.007>.
- [46] S. Cho, J.W. Jang, J.S. Lee, K.H. Lee, Porous ZnO-ZnSe nanocomposites for visible light photocatalysis, *Nanoscale* 4 (2012) 2066–2071, <https://doi.org/10.1039/c2nr11869f>.
- [47] A. Khorsand Zak, W.H. Abd Majid, M.E. Abrishami, R. Yousefi, X-ray analysis of ZnO nanoparticles by Williamson-Hall and size-strain plot methods, *Solid State Sci.* 13 (2011) 251–256, <https://doi.org/10.1016/j.solidstatesciences.2010.11.024>.
- [48] M.H. Hong, H. Choi, D. Il Shim, H.H. Cho, J. Kim, H.H. Park, Study of the effect of stress/strain of mesoporous Al-doped ZnO thin films on thermoelectric properties, *Solid State Sci.* 82 (2018) 84–91, <https://doi.org/10.1016/j.solidstatesciences.2018.05.010>.
- [49] M.T. Chowdhury, M.A. Zubair, H. Takeda, K.M.A. Hussain, M.F. Islam, Optical and structural characterization of ZnSe thin film fabricated by thermal vapour deposition technique, *ALMS Mater Sci* 4 (2017) 1095–1121, <https://doi.org/10.3934/matersci.2017.5.1095>.
- [50] H. Liu, Y. Hu, X. He, H. Jia, X. Liu, B. Xu, In-situ anion exchange fabrication of porous ZnO/ZnSe heterostructural microspheres with enhanced visible light photocatalytic activity, *J. Alloys Compd.* 650 (2015) 633–640, <https://doi.org/10.1016/j.jallcom.2015.08.001>.
- [51] S. Cho, J.W. Jang, S.H. Lim, H.J. Kang, S.W. Rhee, J.S. Lee, K.H. Lee, Solution-based fabrication of ZnO/ZnSe heterostructure nanowire arrays for solar energy conversion, *J. Mater. Chem.* 21 (2011) 17816–17822, <https://doi.org/10.1039/cljm14014k>.
- [52] S. Ghose, D. Jana, Defect dependent inverted shift of band structure for ZnO nanoparticles, *Mater. Res. Express* 6 (2019), 105907.
- [53] W.W. Zhong, F.M. Liu, L.G. Cai, X.Q. Liu, Y. Li, Effect of growth time on the structure, Raman shift and photoluminescence of Al and Sb codoped ZnO nanorod ordered array thin films, *Appl. Surf. Sci.* 257 (2011) 9318–9322, <https://doi.org/10.1016/j.apsusc.2011.05.032>.
- [54] B. Sotillo, G. Escalante, C. Radoi, V. Muñoz-Sanjosé, J. Piñeras, P. Fernández, Correlative study of structural and optical properties of ZnSe under severe plastic deformation, *J. Appl. Phys.* 126 (2019), <https://doi.org/10.1063/1.5128878>.
- [55] P. Sadhukhan, M. Kundu, S. Rana, R. Kumar, J. Das, P.C. Sil, Microwave induced synthesis of ZnO nanorods and their efficacy as a drug carrier with profound anticancer and antibacterial properties, *Toxicol Rep* 6 (2019) 176–185, <https://doi.org/10.1016/j.toxrep.2019.01.006>.
- [56] M. Acheboune, M. Khenfouch, I. Boukhoubza, L. Leontie, C. Doroftei, A. Carlescu, G. Bulai, B. Mothudi, I. Zorkani, A. Jorio, Microstructural, FTIR and Raman spectroscopic study of Rare earth doped ZnO nanostructures, *Mater. Today: Proc.* (2021), <https://doi.org/10.1016/j.mtpr.2021.04.144>.
- [57] T. Gupta, R.P. Chauhan, Structural, morphological, and electrical properties of ZnSe nanostructures: effects of Zn precursors, *Surface. Interfac.* 25 (2021), 101196, <https://doi.org/10.1016/j.surfin.2021.101196>.
- [58] I. Němec, I. Císařová, Z. Mička, Study of the family of glycine-selenious acid addition compounds: crystal structure of diglycine hydrogen selenite and vibrational spectra and DSC measurement of diglycine hydrogen selenite and monoglycine-selenious acid crystals, *J. Solid State Chem.* 140 (1998) 71–82, <https://doi.org/10.1006/jssc.1998.7855>.
- [59] M. Chen, L. Gao, Synthesis and characterization of wurtzite ZnSe one-dimensional nanocrystals through molecular precursor decomposition by solvothermal method, *Mater. Chem. Phys.* 91 (2005) 437–441, <https://doi.org/10.1016/j.matchemphys.2004.12.005>.
- [60] S. Akhmal Saadon, P. Sathishkumar, A.R. Mohd Yusoff, M.D. Hakim Wirzal, M. T. Rahmalan, H. Nur, Photocatalytic activity and reusability of ZnO layer synthesised by electrolysis, hydrogen peroxide and heat treatment, *Environ. Technol.* 37 (2016) 1875–1882, <https://doi.org/10.1080/0959330.2015.1135989>.
- [61] T.R. Giraldo, G.V.F. Santos, V.R. Mendonça, C. Ribeiro, I.T. Weber, Annealing effects on the photocatalytic activity of ZnO nanoparticles, *J. Nanosci. Nanotechnol.* 11 (2011) 3635–3640.
- [62] J. He, W. Wang, X. Zheng, Y. Cao, L. Kong, Y. Wu, Z. Wu, J. Kang, Enhanced photocatalytic efficiency of ZnO/ZnSe coaxial nanowires through interfacial strain modification, *Physica E Low Dimens Syst Nanostruct* 103 (2018) 430–434, <https://doi.org/10.1016/j.physe.2018.06.029>.
- [63] C.S. Lee, K.A. Matori, S.H. Ab Aziz, H. Mohamed Kamari, I. Ismail, M.H. Mohd Zaid, Influence of zinc oxide on the physical, structural and optical band gap of zinc silicate glass system from waste rice husk ash, *Optik* 136 (2017) 129–135, <https://doi.org/10.1016/j.ijleo.2017.02.034>.
- [64] W. Chen, N. Zhang, M.Y. Zhang, X.T. Zhang, H. Gao, J. Wen, Controllable growth of ZnO-ZnSe heterostructures for visible-light photocatalysis, *CrystEngComm* 16 (2014) 1201–1206, <https://doi.org/10.1039/c3ce42068j>.
- [65] R. Chen, J. Wang, S. Luo, L. Xiang, W. Li, D. Xie, Unraveling photoexcited electron transfer pathway of oxygen vacancy-enriched ZnO/Pd hybrid toward visible light-enhanced methane detection at a relatively low temperature, *Appl. Catal., B* 264 (2020), 118554.
- [66] F. Yu, Z. Liu, Y. Li, D. Nan, B. Wang, L. He, J. Zhang, X. Tang, H. Duan, Y. Liu, Effect of oxygen vacancy defect regeneration on photocatalytic properties of ZnO nanorods, *Appl. Phys. A* 126 (2020) 1–12.
- [67] S.S. Patil, M.G. Mali, M.S. Tamboli, D.R. Patil, M. V. Kulkarni, H. Yoon, H. Kim, S. S. Al-Deyab, S.S. Yoon, S.S. Kolekar, B.B. Kale, Green approach for hierarchical nanostructured Ag-ZnO and their photocatalytic performance under sunlight, *Catal. Today* 260 (2016) 126–134, <https://doi.org/10.1016/j.cattod.2015.06.004>.
- [68] B.A. Taleati, L. Cozzarini, B. Olofinjana, G. Bertolini, S.A. Adewinbi, S. Behrendt, Preparation of nanocrystalline ZnO/CoxOy and CNT/CoxOy bilayers for photoabsorption potential: XPS and some surface structural characterization, *Mater. Sci. Semicond. Process.* 87 (2018) 155–161, <https://doi.org/10.1016/j.mss.2018.07.012>.
- [69] S.C. Dixon, S. Sathasivam, B.A.D. Williamson, D.O. Scanlon, C.J. Carmalt, I. P. Parkin, Transparent conducting n-type ZnO: Sc-synthesis, optoelectronic properties and theoretical insight, *J Mater Chem C Mater* 5 (2017) 7585–7597.
- [70] C. Li, Y. Wang, S. Chen, W. Zhang, Z. Wang, Z. Hou, Enhanced photoelectrochemical performance based on conformal and uniform ZnO/ZnSe/CdS heterostructures on Zn foil substrate, *Int. J. Hydrogen Energy* 45 (2020) 8257–8272, <https://doi.org/10.1016/j.ijhydene.2020.01.069>.
- [71] R. Islam, D.R. Rao, X-ray photoelectron spectroscopy of Zn1–xCdSe thin films, *J. Electron. Spectrosc. Relat. Phenom.* 81 (1996) 69–77, [https://doi.org/10.1016/0368-2048\(95\)02551-0](https://doi.org/10.1016/0368-2048(95)02551-0).
- [72] M. Bordbar, N. Negahdar, M. Nasrollahzadeh, L. Melissa Officinalis, Leaf extract assisted green synthesis of CuO/ZnO nanocomposite for the reduction of 4-nitrophenol and Rhodamine B, *Sep. Purif. Technol.* 191 (2018) 295–300, <https://doi.org/10.1016/j.seppur.2017.09.044>.
- [73] H.-L. Cao, C. Liu, F.-Y. Cai, X.-Y. Qiao, A.B. Dichiara, C. Tian, J. Lü, In situ immobilization of ultra-fine Ag NPs onto magnetic Ag@RF@Fe3O4 core-satellite nanocomposites for the rapid catalytic reduction of nitrophenols, *Water Res.* 179 (2020), 115882.
- [74] S. Ibrahim, S. Chakrabarty, S. Ghosh, T. Pal, Reduced graphene oxide – zinc sulfide composite for solar light responsive photo current generation and photocatalytic 4-nitrophenol reduction, *ChemistrySelect* 2 (2017) 537–545, <https://doi.org/10.1002/slct.201601999>.
- [75] N.K.R. Bogireddy, P. Sahare, U. Pal, S.F.O. Méndez, L.M. Gomez, V. Agarwal, Platinum nanoparticle-assembled porous biogenic silica 3D hybrid structures with outstanding 4-nitrophenol degradation performance, *Chem. Eng. J.* 388 (2020), 124237, <https://doi.org/10.1016/j.cej.2020.124237>.
- [76] J.Q. Ma, X.H. Guo, Y.Y. Zhang, H.G. Ge, Catalytic performance of TiO2@Ag composites prepared by modified photodeposition method, *Chem. Eng. J.* 258 (2014) 247–253, <https://doi.org/10.1016/j.cej.2014.06.120>.
- [77] E.M. Flores, R.A. Gouvea, M.J. Piotrowski, M.L. Moreira, Band alignment and charge transfer predictions of ZnO/ZnX (X = S, Se or Te) interfaces applied to solar cells: a PBE+U theoretical study, *Phys. Chem. Chem. Phys.* 20 (2018) 4953–4961, <https://doi.org/10.1039/c7cp0177d>.
- [78] Y. Zhang, J. Liu, M. Singh, E. Hu, Z. Jiang, R. Raza, F. Wang, J. Wang, F. Yang, B. Zhu, Superionic conductivity in ceria-based heterostructure composites for low-temperature solid oxide fuel cells, *Nano-Micro Lett.* 12 (2020) 1–20, <https://doi.org/10.1007/s40820-020-00518-x>.
- [79] X. Wang, C. Li, Roles of phase junction in photocatalysis and photoelectrocatalysis, *J. Phys. Chem. C* 122 (2018) 21083–21096, <https://doi.org/10.1021/acs.jpcc.8b06039>.
- [80] J. Liu, N. Ma, W. Wu, Q. He, Recent progress on photocatalytic heterostructures with full solar spectral responses, *Chem. Eng. J.* 393 (2020), 124719, <https://doi.org/10.1016/j.cej.2020.124719>.
- [81] M.F. Ehsan, S. Bashir, S. Hamid, A. Zia, Y. Abbas, K. Umbreen, M.N. Ashiq, A. Shah, One-pot facile synthesis of the ZnO/ZnSe heterostructures for efficient photocatalytic degradation of azo dye, *Appl. Surf. Sci.* 459 (2018) 194–200, <https://doi.org/10.1016/j.apsusc.2018.07.162>.